Supplementary Information

Light-induced modulation of DNA recognition by the Rad4/XPC damage sensor protein

Amirrasoul Tavakoli[1], Debamita Paul[1], Hong Mu[2],

Jagannath Kuchlyan[1‡], Saroj Baral[3], Anjum Ansari[3], Suse Broyde[2], Jung-Hyun Min[1†]

[1]Department of Chemistry and Biochemistry, Baylor University, Waco, TX 76706, USA

[2]Department of Biology, New York University, New York, NY 10003, USA

[3]Department of Physics, University of Illinois at Chicago, Chicago, IL 60607, USA

[†] To whom correspondence may be addressed

[‡] Current address: Department of Chemistry, University of Oxford, Oxford, OX1 3TA, UK

Tel: (254)710-2095

E-mail: JungHyun_Min@baylor.edu

Supplementary Methods

Experimental setup for fluorescence lifetime measurements. The fluorescence decays of DNA labeled with tC^o and tC_{nitro} were measured using a time-correlated single-photon counting (TCSPC) system (DeltaFlex, HORIBA) equipped with a Ti-sapphire laser source with a tunable range from 690 to 1040 nm (Mai Tai HP, Spectra-Physics). We used ~100 fs pulses centered at 730 nm with a repetition rate of 80 MHz and average power 1.8 W (~23 nJ/pulse). The fundamental beam (730 nm) was passed through a half-wave plate and then to a pulse picker for reducing the repetition rate of the beam from 80 MHz to 4 MHz. For the second harmonic generation, the fundamental 730 nm beam coming from the pulse picker was focused onto a thin β-barium borate (BBO) crystal in second-harmonic generator (Minioptics, Inc., Arcadia, CA), which generated a frequency-doubled beam centered at 365 nm. The remaining fundamental beam and frequency-doubled 365 nm beam were separated through a dichroic mirror. The fundamental pulse was given a time delay through an optical delay cable connected with a delay box. The residual fundamental was allowed to pass through a photodiode for triggering the start signal in the DeltaFlex system. For excitation of tC^o, the laser pulses were passed through a monochromator set at 365 nm (band pass 10 nm) attached to the DeltaFlex setup. We used neutral density filter (FSQ-ND20, broadband UV-grade fused silica metallic filter, Newport corporation) to reduce power of the excitation light suitable for TCSPC measurements. The intensity of the laser delivered to the samples was 0.21 mW/cm^2 as measured by a General Tools Digital UVA/UVB Meter, 280-400 nm (#UV513AB). The fluorescence from the samples passed through a long pass filter cut at 375 nm and the signal was collected at magic angle with the emission polarizer oriented 54.7 ° from the direction of the excitation polarizer, chosen as vertical. This magic angle configuration removes any depolarization effects in the measured fluorescence decay curves from the rotational dynamics of the labeled biomolecules that could be present when exciting with polarized laser pulses, and is the configuration recommended by Horiba for their fluorescence lifetime setups. The transmitted signal was passed through the entrance slit of emission monochromator set at 470 nm (band pass 10 nm) and collected by a Picosecond Photon Detection single-photon counting module (PPD-850, Horiba). The instrument response function (IRF) of the system was measured using a dilute aqueous solution (3% w/w) of LUDOX AM colloidal silica (Sigma-Aldrich). The full-width half maxima (FWHM) was ~425 ps. Fluorescence decay curves were recorded on a 100 ns timescale, resolved into 4,096 channels, to a total of 10,000 counts in the peak channel. For temperature

control, the temperature of the sample chamber was regulated by Quantum Northwest Peltier-Controlled TC 1.

Lesion structure modeling, optimization and initial models

The initial models of NPOM-dT were built at the center dT of a 13-mer B-DNA sequences (nucleotide steps 10 – 23, AT1 sequence **Table 1** in the main text) in either a major groove or a base-displaced intercalated conformation using Discovery Studio 2.5 (Accelrys Software Inc.). Six major groove and four base-displaced intercalated conformations that can fit in the B-DNA were obtained (**Figure S13**). The 10 candidate NPOM-dT structures were then geometry optimized in Polarizable Continuum Model (PCM) of water at HF/6-31G* level of theory using Gaussian 09[1]. Five optimized NPOM-dT structures (four in the major groove and one intercalated) were modeled into the 13-mer B-DNA without extensive distortions to the duplex, and were used as the initial models of lesion-containing DNA duplex (**Figure S14**). The 13-mer B-DNA was used as the initial model of the unmodified duplex.

Force field parameterization

We used ff14SB[2] and GAFF[3] force field for all MD simulations. The missing parameters for the NPOM-dT lesion were assigned utilizing similar values in GAFF force field and the values given in Myung *et al.*[4]. Electrostatic potentials for the five NPOM-dT conformations in the initial models were calculated at the HF/6-31G* level of theory using Gaussian 09[1]. The partial charges for the NPOM-dT lesion were obtained using a multiconformational restrained electrostatic potential (RESP) fit procedure[5]. The partial charges, together with atom types and additional parameters, are given in **Table S3.**

Water box and counterions

The initial DNA models were neutralized with Na^+ counterions and solvated with explicit TIP3P water[6] in a cubic periodic box with side length of 63.0 Å using the tLEAP module of the AMBER18 suite of programs [7].

MD simulation

All MD simulations were carried out using the AMBER18 suite of programs[7]. The Particle-Mesh Ewald method [8] with 9.0 Å cutoff for the non-bonded interactions was used in the energy minimizations and MD simulations. Minimizations were carried out in three stages. First, 500 steps of steepest descent minimization followed by 500 cycles of conjugate gradient

minimization were conducted for the water molecules and counterions with a restraint force constant of 50 kcal/(mol·Å^2) on the solute molecules. Then, 500 steps of steepest descent minimization followed by 500 cycles of conjugate gradient minimization were carried out for the water molecules and counterions with a restraint force constant of 10 kcal/(mol·Å^2) on the solute molecules. In the last round, 500 steps of steepest descent minimization followed by 500 cycles of conjugate gradient minimization were carried out on the whole system without restraints. The minimized structures were then subjected to three rounds of equilibration. First, each system was equilibrated at constant temperature of 10º K for 30 ps with the solute molecules fixed with a restraint force constant of 50 kcal/(mol·Å^2). Then the system was heated from 10º K to 300º K over 300 ps with the solute molecules fixed with a restraint force constant of 50 kcal/(mol·Å^2) at constant volume. In the last round of equilibration, the restraint force constant on the solute was reduced through three steps: at 10 kcal/(mol·Å^2) for 200 ps, at 1 kcal/(mol·Å^2) for 200 ps, and then at 0.1 kcal/(mol·Å^2) for 200 ps with constant pressure at 300º K. Following equilibration, production MD simulations for each system were carried out in a constant-temperature, constant-pressure (NPT) ensemble at 300 K and 1 atm for 1.5 μs. The temperature was controlled with a Langevin thermostat [9] with a 5 ps^{-1} collision frequency. The pressure was maintained with the Berendsen coupling method [10]. A 2.0 fs time step and the SHAKE algorithm [11] were applied in all MD simulations. A 1 kcal/mol restraint was applied to the end base pair hydrogen bond donor and acceptor heavy atom pairs during the production MDs.

Structural analyses

Lesion containing 6-mer RMSD. In order to evaluate the overall stability of the 6-mer sequence that includes the base pair steps for the FRET pairs at two ends (nucleotide steps 14 – 19, AT1 sequence **Table 1** in the main text), we calculated the RMSD for the heavy atoms of the 6-mer sequence excluding the lesion-containing nucleotide. The structural ensembles were fitted to the first frame of each MD trajectory at the heavy atoms of the two nucleotide steps on each end of the 6-mer sequence. The 6-mer RMSD were calculated for the heavy atoms of the 6-mer excluding the lesion-containing nucleotide without fitting using cpptraj module of AMBER18[7]. During the MD simulations, three trajectories started from varying major groove conformations and one trajectory started from a base-displaced intercalated conformation achieved stable conformation for the 6-mer sequence. One trajectory started from a major groove conformation

exhibited ruptured lesion site and extensive distortions to the 6-mer (**Figure S15**), and hence was excluded from further structural analyses.

Lesion conformation clustering. We measured 4 torsion angles that determine the lesion conformation (**Figure S16**) using cpptraj module of AMBER18[7]. The D1, D2, D3, and D4 torsion angles were clustered into 2, 3, 3, and 3 groups respectively using k-means method with Euclidean distance. 42 unique combinations of all torsion angle clusters were obtained. The top 10 clusters included over 96% of total population and each cluster had a population fraction of at least 1% (**Figure S16**). Two predominant conformational clusters appeared repeatedly in all trajectories for the major groove conformations, and one predominant cluster occurred for the base-displaced intercalated conformation; these were collected for further analyses.

Best representative structures. The best representative structure for each clustered conformational ensemble is defined as the one frame that has the lowest 6-mer RMSD value (see *Lesion containing 6-mer RMSD*) to all other frames.

Hydrogen bond occupancy. Hydrogen bonds occupancies for the two base pairs on each side of the NPOM-dT site and respective base pairs in the unmodified DNA were calculated using the cpptraj module of AMBER18[7], with a hydrogen bond (heavy-light-heavy atom) angle cutoff of $\geq 145°$ and a heavy-to-heavy atom distance cutoff of ≤ 3.3 Å.

FRET efficiency calculation. In order to estimate the distance and angle between designed FRET pair and the efficiency values, we modeled the rings of the FRET pair (tC^o and tC_{nitro}) into the DNA duplexes. We used a tC^o structure (PDB ID: 3QNO[12]) to mimic the tC_{nitro} rings and superposed it to the cytosine ring at the acceptor position. We replaced the dG at the donor position with a dC by superposition at the sugar ring and then superposed another tC^o to the cytosine ring at this position. The distance between the FRET pair ("PD distance") is defined as the distance between the center of mass (COM) for the middling ring of each tC^o model. The dihedral angles between the dipoles of the FRET pair ("dipole dihedral angle") were obtained by adjusting the dihedral angle between the y axes of the two base pair planes with relative angles between each dipole and its y axis, and reflects the twist between the base pair steps. The vectors used for the calculation of FRET efficiency were defined as in Preus *et al.*[13]

Block average analyses. The PD distance and dipole dihedral angle for the two predominant major-groove and one base-displaced intercalated NPOM-dT ensembles and the unmodified

DNA ensemble were analyzed using the block averaging method [14, 15]. In brief, the time series data were divided into "blocks" with a block size that exceeds the longest correlation time, 20 ns in these cases. The average for each block was computed and termed "block average". The mean values and the standard deviations of the block averages were used to represent the average and the variance of averages.

Molecular structures were rendered using PyMOL 1.3.x (Schrodinger, LLC.). All MD simulation data were plotted using MATLAB 7.10.0 (The MathWorks, Inc.).

Supplementary Tables S1-S2

Table S1. Fluorescence lifetimes and FRET efficiencies from DE analyses.

	τ_1	A_1	E_1	τ_2	A_2	E_2	τ_3	A_3	E_3	τ_4	A_4	E_4	<E>
AT7_DA	0.280 ± 0.002	0.790 ± 0.018	0.944 ± 0.000				1.410 ± 0.107	0.119 ± 0.009	0.722 ± 0.021	4.873 ± 0.081	0.089 ± 0.009	0.042 ± 0.016	0.837 ± 0.012
AT7_DA + Rad4	0.166 ± 0.067	0.642 ± 0.046	0.967 ± 0.013	0.528 ± 0.103	0.234 ± 0.066	0.896 ± 0.020	2.299 ± 0.106	0.080 ± 0.010	0.548 ± 0.020	5.260 ± 0.039	0.043 ± 0.011	-0.033 ± 0.007	0.873 ± 0.025
AT7_DA + $h\nu$	0.266 ± 0.006	0.850 ± 0.000	0.946 ± 0.001				1.871 ± 0.152	0.083 ± 0.005	0.632 ± 0.030	5.333 ± 0.137	0.066 ± 0.005	-0.048 ± 0.029	0.854 ± 0.001
AT7_DA + $h\nu$ + Rad4	0.267 ± 0.004	0.856 ± 0.005	0.947 ± 0.008				2.057 ± 0.070	0.086 ± 0.005	0.595 ± 0.013	5.657 ± 0.140	0.056 ± 0.005	-0.111 ± 0.027	0.857 ± 0.002
AT10_DA	0.251 ± 0.008	0.867 ± 0.005	0.950 ± 0.001				1.930 ± 0.052	0.073 ± 0.005	0.620 ± 0.010	5.139 ± 0.049	0.059 ± 0.000	-0.009 ± 0.009	0.869 ± 0.004
AT10_DA + Rad4	0.261 ± 0.005	0.847 ± 0.004	0.948 ± 0.001				2.004 ± 0.072	0.079 ± 0.005	0.606 ± 0.014	5.216 ± 0.030	0.073 ± 0.005	-0.024 ± 0.006	0.850 ± 0.006

DNA_D	$\langle\tau_D\rangle$
AT7_D	3.847 ± 0.132
AT7_D + $h\nu$	5.129 ± 0.049
AT10_D	5.083 ± 0.017

The errors indicate the s.d. of the data points from three independent samples.

Table S2. Fluorescence lifetimes and FRET efficiencies from MEM analyses

	τ_1	A_1	E_1	τ_2	A_2	E_2	τ_3	A_3	E_3	τ_4	A_4	E_4	<E>
AT7_DA	0.309 ± 0.006	0.742 ± 0.037	0.939 ± 0.001				1.768 ± 0.087	0.125 ± 0.012	0.653 ± 0.017	4.806 ± 0.075	0.131± 0.026	0.058 ± 0.014	0.785 ± 0.028
AT7_DA + Rad4	0.157 ± 0.015	0.545 ± 0.029	0.969 ± 0.003	0.391 ± 0.007	0.306 ± 0.035	0.923 ± 0.001	1.705 ± 0.025	0.082 ± 0.002	0.665 ± 0.005	4.673 ± 0.006	0.065 ± 0.005	0.080 ± 0.006	0.870 ± 0.004
AT7_DA + $h\nu$	0.214 ± 0.014	0.892 ± 0.007	0.957 ± 0.002				2.237 ± 0.051	0.052 ± 0.008	0.561 ± 0.010	5.363 ± 0.064	0.054 ± 0.000	-0.051 ± 0.012	0.874 ± 0.004
AT7_DA + $h\nu$ + Rad4	0.202 ± 0.009	0.902 ± 0.003	0.960 ± 0.001				2.414 ± 0.145	0.053 ± 0.007	0.526 ± 0.028	5.502 ± 0.308	0.043 ± 0.007	-0.078 ± 0.060	0.877 ± 0.002
AT10_DA	0.265 ± 0.000	0.863 ± 0.000	0.948 ± 0.000				1.830 ± 0.007	0.068 ± 0.000	0.641 ± 0.001	4.846 ± 0.005	0.068 ± 0.000	0.050 ± 0.001	0.863 ± 0.000
AT10_DA + Rad4	0.231 ± 0.011	0.855 ± 0.009	0.954 ± 0.002				1.841 ± 0.097	0.065 ± 0.003	0.639 ± 0.019	4.915 ± 0.048	0.076 ± 0.002	0.036 ± 0.009	0.861 ± 0.002

DNA_D	$<\tau_D>$
AT7_D	3.773 ± 0.066
AT7_D + $h\nu$	5.142 ± 0.012
AT10_D	5.102 ± 0.078

The errors indicate the s.d. of the data points from three independent samples.

Table S3. Atom names, types, topologies, partial charges and added force field parameters for the NPOM-dT lesion.

Name	Tpye	Topology	Partial charge
P	P	M	1.440501
OP1	O2	E	-0.787291
OP2	O2	E	-0.787291
O5'	OS	M	-0.625530
C5'	CT	M	0.067372
H5'1	H1	E	0.054210
H5'2	H1	E	0.054210
C4'	CT	M	0.108084
H4'	H1	E	0.098912
O4'	OS	S	-0.341532
C1'	CT	B	0.162803
H1'	H2	E	0.082150
N1	N*	B	-0.031648
C2	C	S	0.428169
O2	O	E	-0.454600
C6	CM	B	-0.266057
H6	H4	E	0.227272
C5	CM	B	0.009607
C7	CT	3	-0.248599
H71	HC	E	0.084802
H72	HC	E	0.084802
H73	HC	E	0.084802
C4	C	B	0.499678
O4	O	E	-0.509627
N3	N*	S	-0.113688
CN7	CT	3	0.047549
HN10	HC	E	0.093631
HN11	HC	E	0.093631
ON3	OS	S	-0.325625
CN8	CT	3	0.241184
HN9	HC	E	0.045944
CN16	CT	3	-0.237315
HN1	HC	E	0.077286
HN2	HC	E	0.077286
HN3	HC	E	0.077286
CN9	CA	S	-0.019163
CN14	CA	B	-0.376606
HN7	HA	E	0.207499
CN13	CA	S	0.372688
ON5	OS	S	-0.383059
CN15	CT	3	0.244021
HN5	HC	E	0.095519
HN6	HC	E	0.095519
ON4	OS	S	-0.378980
CN12	CA	S	0.300725
CN11	CA	B	-0.408040
HN8	HA	E	0.260708
CN10	CA	S	0.004866
NX	no	B	0.778735
OX1	o	E	-0.475488
OX2	o	E	-0.423428
C3'	CT	M	0.176438
H3'	H1	E	0.073690
C2'	CT	B	-0.131850
H2'1	HC	E	0.072944
H2'2	HC	E	0.072944
O3'	OS	M	-0.672050

Added force field parameters

BOND

	K_r	r_{eq}
CA-no	322.6	1.468
CA-OS	372.4	1.373

ANGL

	K_r	θ_{eq}
CA-no-o	68.7	118.10
CA-CA-no	66.9	119.54
CA-CA-OS	69.8	119.20
HC-CT-OS	50.9	108.70
CT-OS-CA	62.4	117.60
CA-CT-OS	67.7	110.51
HC-CT-N*	49.9	109.50
CM-C -N*	70.0	114.10
C -N*-C	70.0	126.40
N*-C -N*	70.0	115.40

DIHE

	# of path	$V_n/2$	γ	n
CA-CA-no-o	4	3.68	180.0	2.000
X -CA-OS-X	2	1.80	180.0	2.000

IMPR

	$V_n/2$	γ	n
CA-o -no-o	7.28	180.0	2.000

Supplementary Figures S1-S17

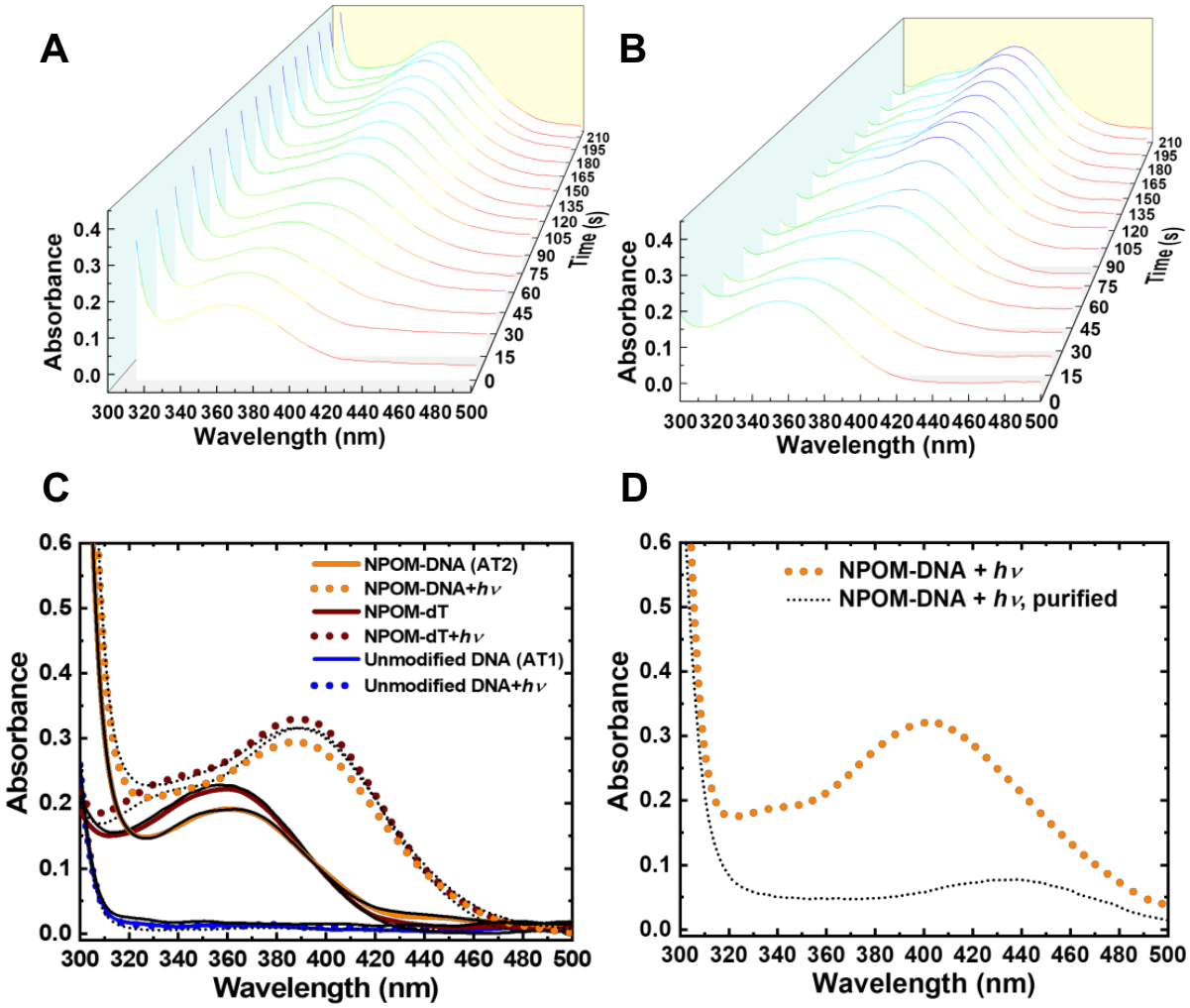

Figure S1. **UV-visible absorption spectroscopy for in situ monitoring of photocleavage of NPOM from DNA and dT nucleoside (A-B)** Absorption spectra of NPOM-modified DNA duplex (NPOM-DNA or AT2; panel A) and NPOM-dT (panel B) were recorded every 15 seconds as the samples were irradiated with light (λ=365 nm) for 210 s. **(C)** Reproducibility of the UV-visible spectra of NPOM-DNA and NPOM-dT before and after photocleavage. Absorption spectra of NPOM-DNA (AT2, orange), NPOM-dT (brown), and unmodified DNA duplex (AT1, blue) before (solid line) and after 120 s of light irradiation (dotted line). Black indicates data from duplicate experiments. **(D)** Absorption spectra of NPOM-DNA after photocleavage irradiation and of the same sample after purification over G-25 size exclusion resin. They show that the purification step effectively removed photocleaved NPOM groups from the DNA.

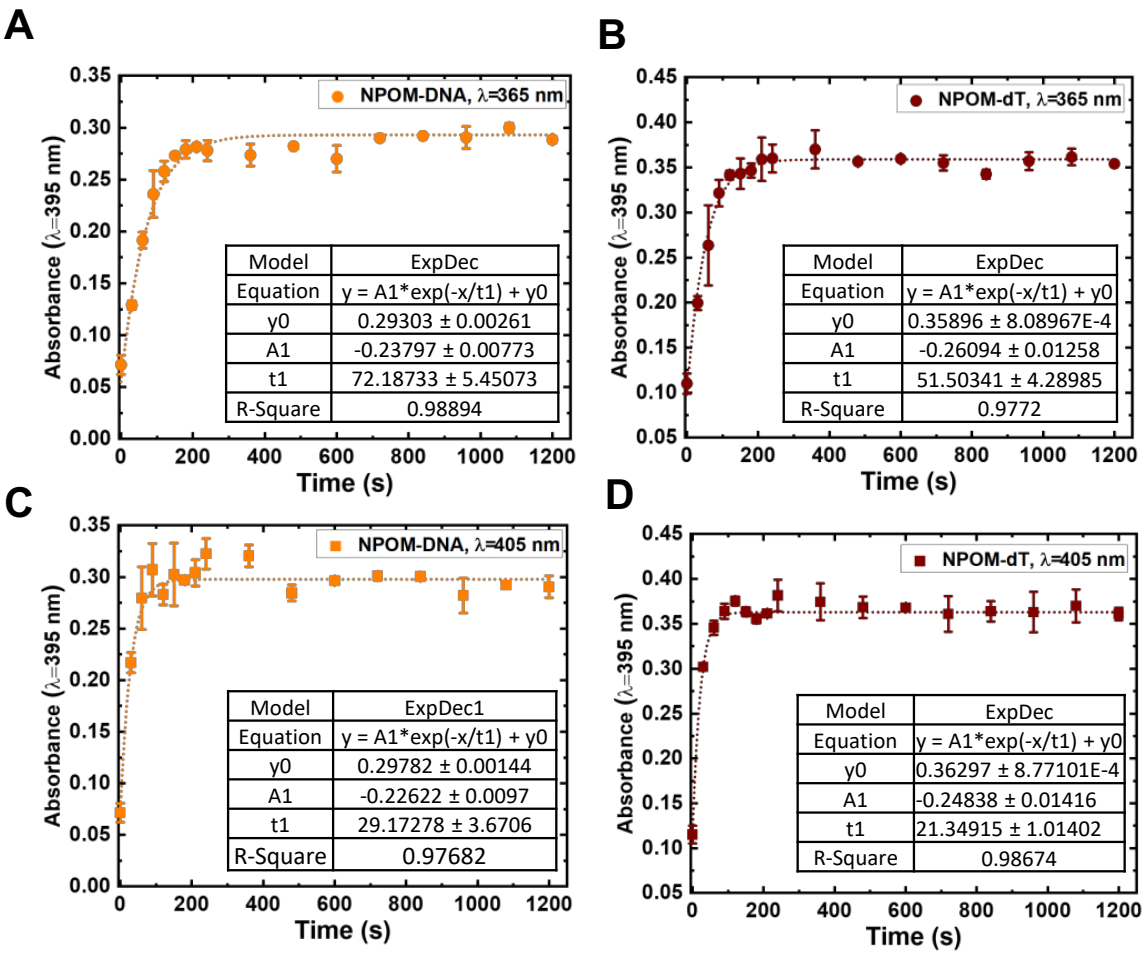

Figure S2. Dose-dependent NPOM photocleavage by 365 nm and 405 nm light. NPOM-DNA and NPOM-dT were irradiated with light at two different wavelengths, λ=365 nm (**A** for NPOM-DNA and **B** for NPOM-dT) and 405 nm (**C** for NPOM-DNA and **D** for NPOM-dT). The time courses of the reaction were monitored by recording the absorption at 395 nm and were analyzed by single exponential fits. The fit equations and parameters are shown in inset for each panel. The concentrations of NPOM-DNA and NPOM-dT used were 40 μM and 45 μM, respectively.

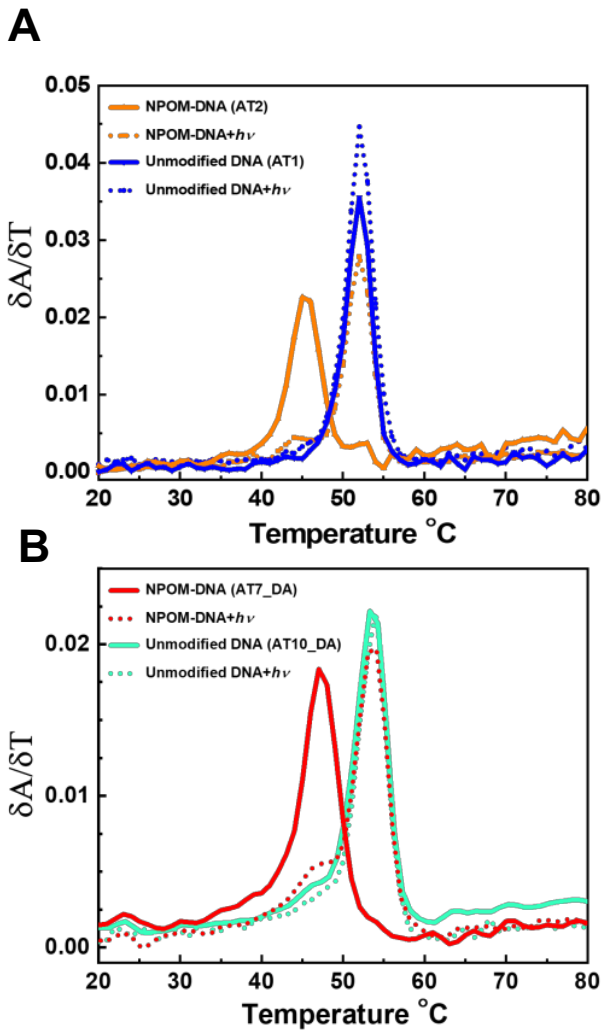

DNA	T_m (°C)
NPOM-DNA (AT2)	45.2 ± 0.2
NPOM-DNA+*hν*	52.0 ± 0.0
Unmodified DNA (AT1)	52.0 ± 0.0
Unmodified DNA+*hν*	52.0 ± 0.1

DNA	T_m (°C)
NPOM-DNA* (AT7_DA)	47.1 ± 0.1
NPOM-DNA*+*hν*	54.0 ± 0.0
Unmodified DNA* (AT10_DA)	53.6 ± 0.5
Unmodified DNA*+*hν*	54.0 ± 0.0

Figure S3. **Thermal melting profiles of DNA duplexes before and after photocleavage.** (*Left*) The first derivatives of the absorbance at 260 nm with respect to temperature (δA/δT) versus temperature. The temperatures at the peak were designated as the T_m. (*Right*) T_m for each construct is reported as the average ± standard deviation (s.d.) of three independent measurements. The uncertainty in T_m as judged by half the temperature interval between successive data points in the derivatives graph is 0.5 °C. **(A)** NPOM-DNA (**AT2**, orange) and the unmodified DNA (**AT1**, blue) before and after irradiation (+hν; λ=365 nm light applied for 3 min.) in solid and dashed lines, respectively. **(B)** DNA with tC°-tC_{nitro} FRET probes: NPOM-DNA* (**AT7**, red) and the unmodified DNA* (**AT10**, green). DNA sequences for each construct are in Table 1.

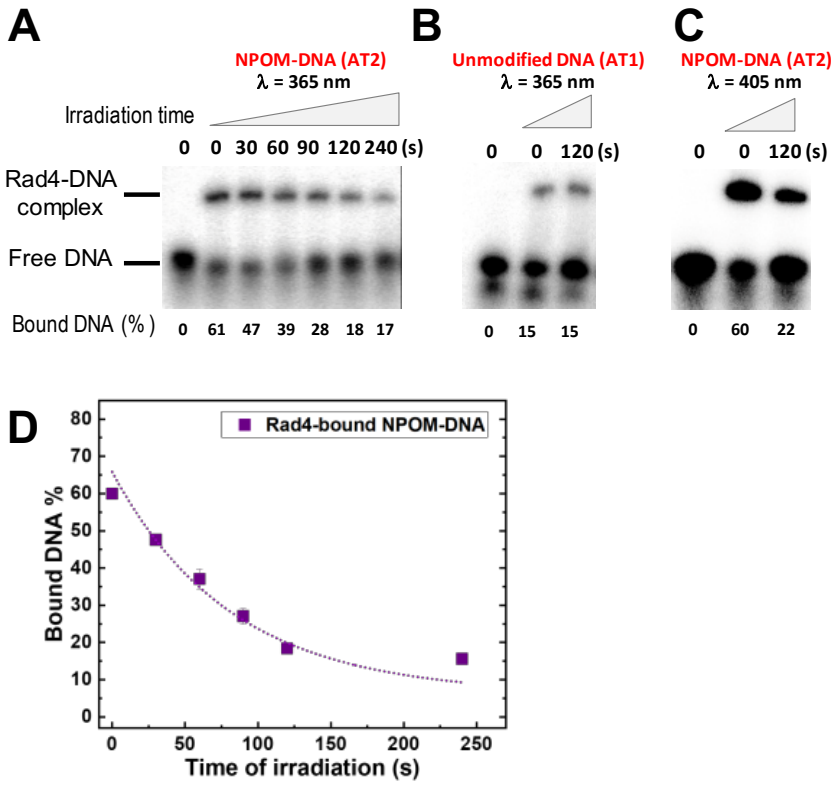

Figure S4. Analyses of Rad4-DNA complexes after co-irradiation. Protein-DNA mixtures were prepared similarly as in the competitive EMSA described in the main text. Each sample contained 5 nM of ^{32}P-labeled NPOM-DNA (AT2, panel **A, C**) or the unmodified control DNA (AT1, panel **B**) and 1000 nM unlabeled competitor DNA (CH7) in the EMSA buffer. After adding 300 nM of protein (or buffer for no-protein control (lane1)), the protein-DNA mixtures were co-irradiated for indicated time periods before being separated on 4.8% native polyacrylamide gels. **(A)** Co-irradiation with 365 nm light decreased the levels of the protein-bound NPOM-DNA over time. **(B)** The same irradiation, however, did not alter the level of protein-bound control DNA. **(C)** Irradiating the NPOM-DNA with 405 nm light also caused similar decrease as with the 365 nm light shown in (A). **(D)** The time course of the change in the protein-bound NPOM-DNA showed kinetics (t_1=82 sec) that were similar to those of the photocleavage reaction monitored by absorbance change at 395 nm (t_1=72 sec) (Figure S2). These results confirm that light applied to induce photocleavage in the samples does not induce nonspecific, erratic crosslinking between the protein and DNA under our experimental conditions.

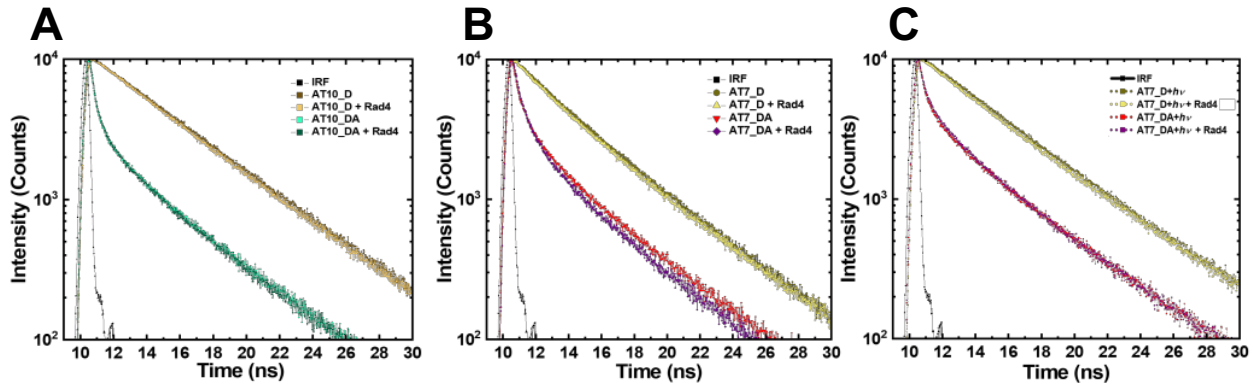

Figure S5. Fluorescence intensity decay curves for DNA_DA and DNA_D with excitation of donor (tC^o**).** Donor/acceptor-labeled DNA_DA without/with Rad4 are shown for **(A)** unmodified DNA (AT10; green/dark green), **(B)** NPOM-DNA (AT7; red/purple) and (**C**) NPOM-DNA after photocleavage (AT7+hv; dotted red/dotted purple). The decay curves for corresponding donor-only labeled DNA_D are in olive (-Rad4) and yellow (+Rad4). The instrument response function (IRF) is shown in black.

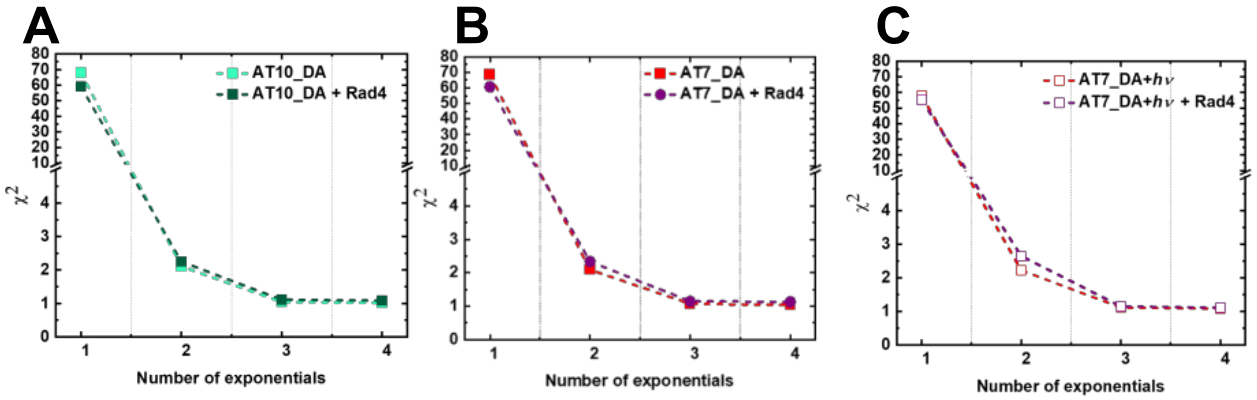

Figure S6. The sum of the residuals χ^2 as a function of increasing number of discrete exponentials. The $\chi 2$ values (defined as $\frac{1}{N}\sum_i \frac{(y_i - y_{fit,i})^2}{\sigma_i^2}$) from a discrete exponential fit to the fluorescence decay profiles versus the number of discrete exponentials used are shown for DNA_DA samples in **(A)** unmodified DNA (AT10_DA) without and with Rad4 (filled green/dark green), **(B)** NPOM-DNA (AT7_DA) without and with Rad4 (filled red/purple) and **(C)** NPOM-DNA after photocleavage (AT7_DA + $h\nu$) without and with Rad4 (empty red/ purple).

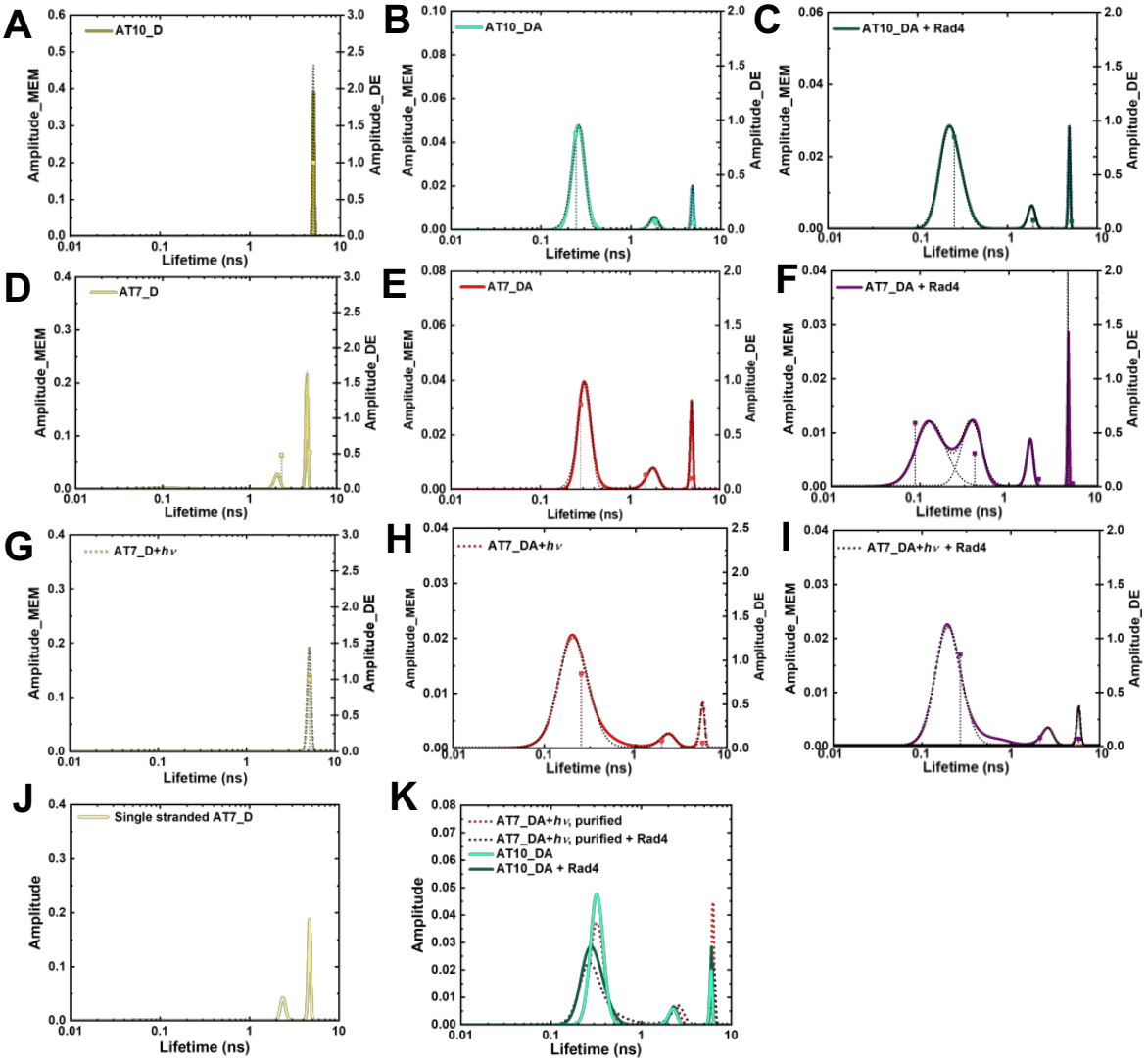

Figure S7. Fluorescence lifetime distributions obtained from maximum entropy method (MEM) are shown together with the lifetimes from discrete exponential (DE) analysis (vertical lines). The fractional amplitudes from the MEM (DE) are indicated on the left (right) y-axis. The Gaussian fittings for MEM distributions are shown in black dotted lines. **(A-C)** Unmodified DNA (AT10), **(D-F)** NPOM-DNA (AT7) and **(G-I)** NPOM-DNA after photocleavage (AT7+$h\nu$). (*A,D,G*) donor-only DNA (DNA_D); (*B,E,H*) donor/acceptor-labeled DNA (DNA_DA) without Rad4; (*C,F,I*) donor/acceptor-labeled DNA with equimolar Rad4. **(J)** single stranded AT7_D; **(K)** AT7_DA+$h\nu$ purified with G25 size exclusion resin, without and with Rad4. Data for AT10_DA without and with Rad4 are also shown for comparison.

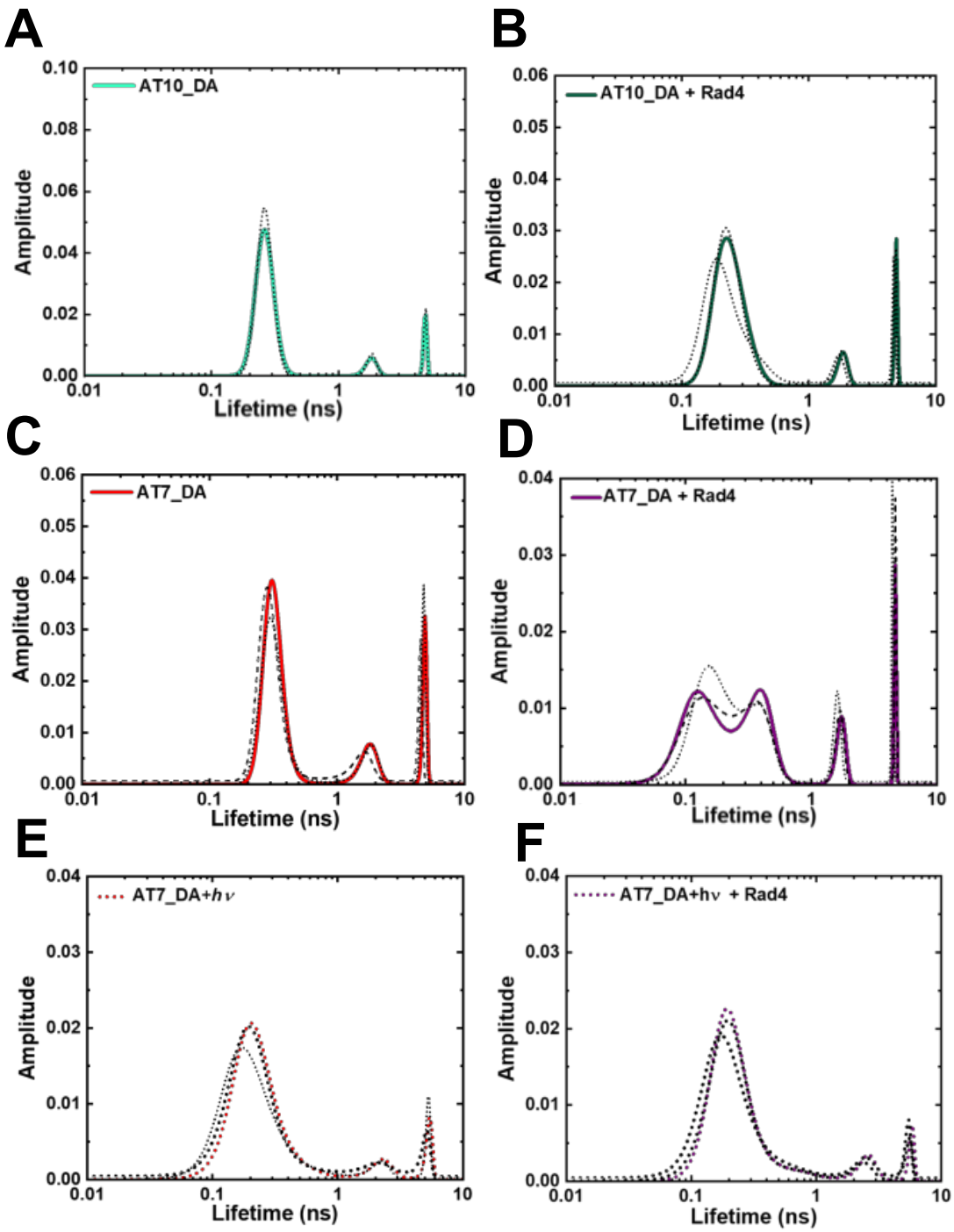

Figure S8. Reproducibility of fluorescence lifetime distributions obtained from MEM analyses. The MEM lifetime distributions from three independent measurements are overlaid in each panel for **(A, B)** unmodified DNA (AT10_DA) in the absence and presence of Rad4, **(C, D)** NPOM-DNA (AT7_DA) in the absence and presence of Rad4, and **(E, F)** NPOM-DNA after photocleavage (AT7_DA + $h\nu$) in the absence and presence of Rad4.

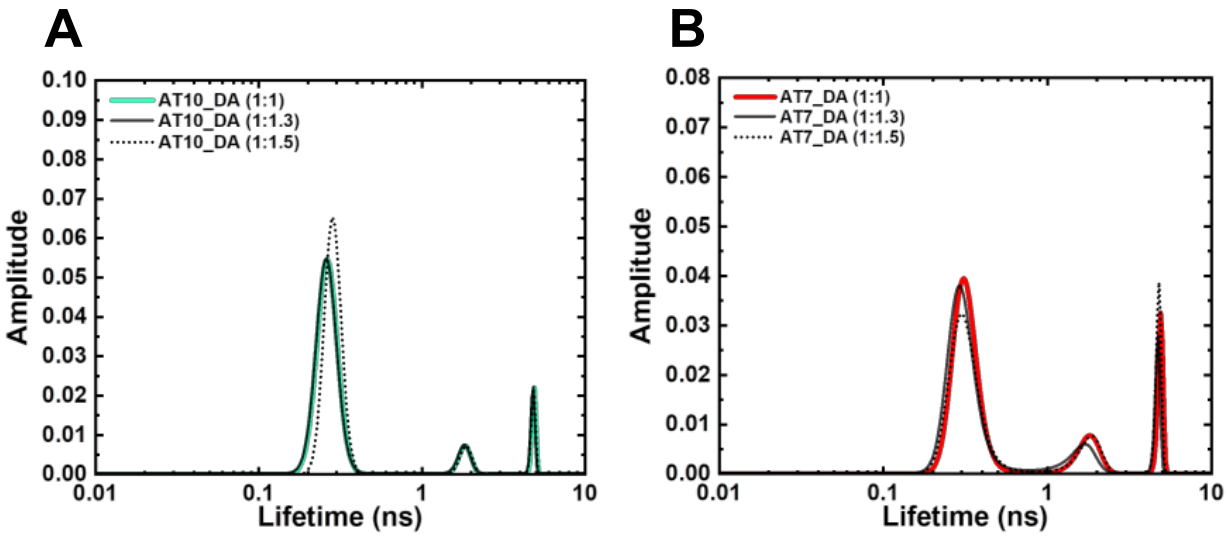

Figure S9. FLT distributions for donor/acceptor-labeled DNA annealed with varying donor:acceptor strand ratios for **(A)** unmodified DNA (AT10_DA, green), **(B)** NPOM-DNA (AT7_DA, red). Donor and acceptor strands are the bottom and top strands of the DNA sequences shown in Table 1, respectively. The FLT distributions remain the same among these samples indicating that the low/zero FRET peak is not due to an excess, unannealed donor strand in the samples.

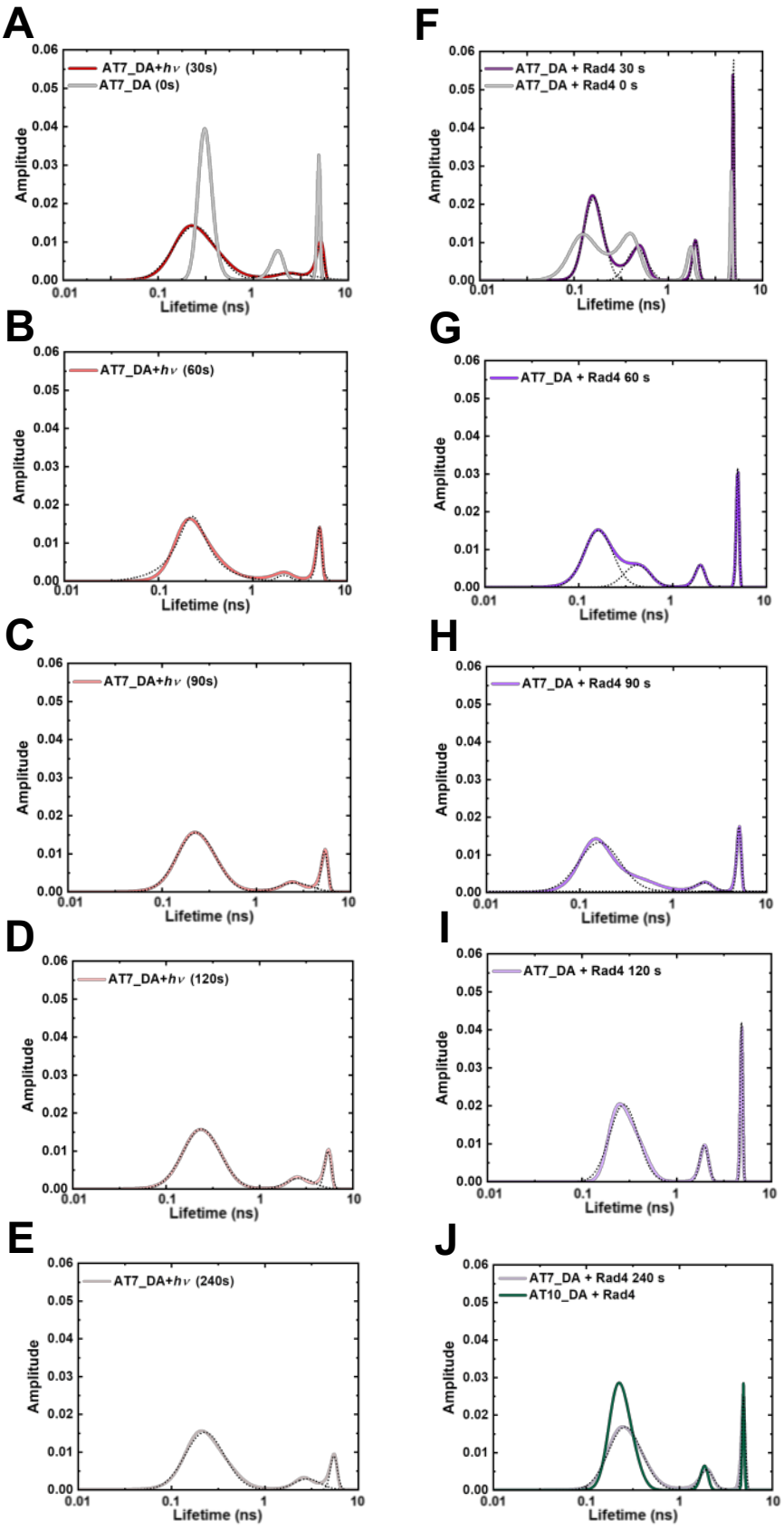

Figure S10. FLT-MEM distributions of NPOM-DNA without or with Rad4, with varying photocleavage irradiation times. NPOM-DNA alone (**A-E**; AT7_DA) or in the presence of equimolar Rad4 (**F-J**; AT7_DA+Rad4) were irradiated by light (λ=365 nm) for various lengths of time. **(A, F)** 0 s and 30 s **(B, G)** 60 s, **(C, H)** 90 s, **(D, I)** 120s, and **(E, J)** 240 s of photo-irradiation**.** (J) also shows unmodified DNA (AT10_DA) + Rad4 in green for comparison.

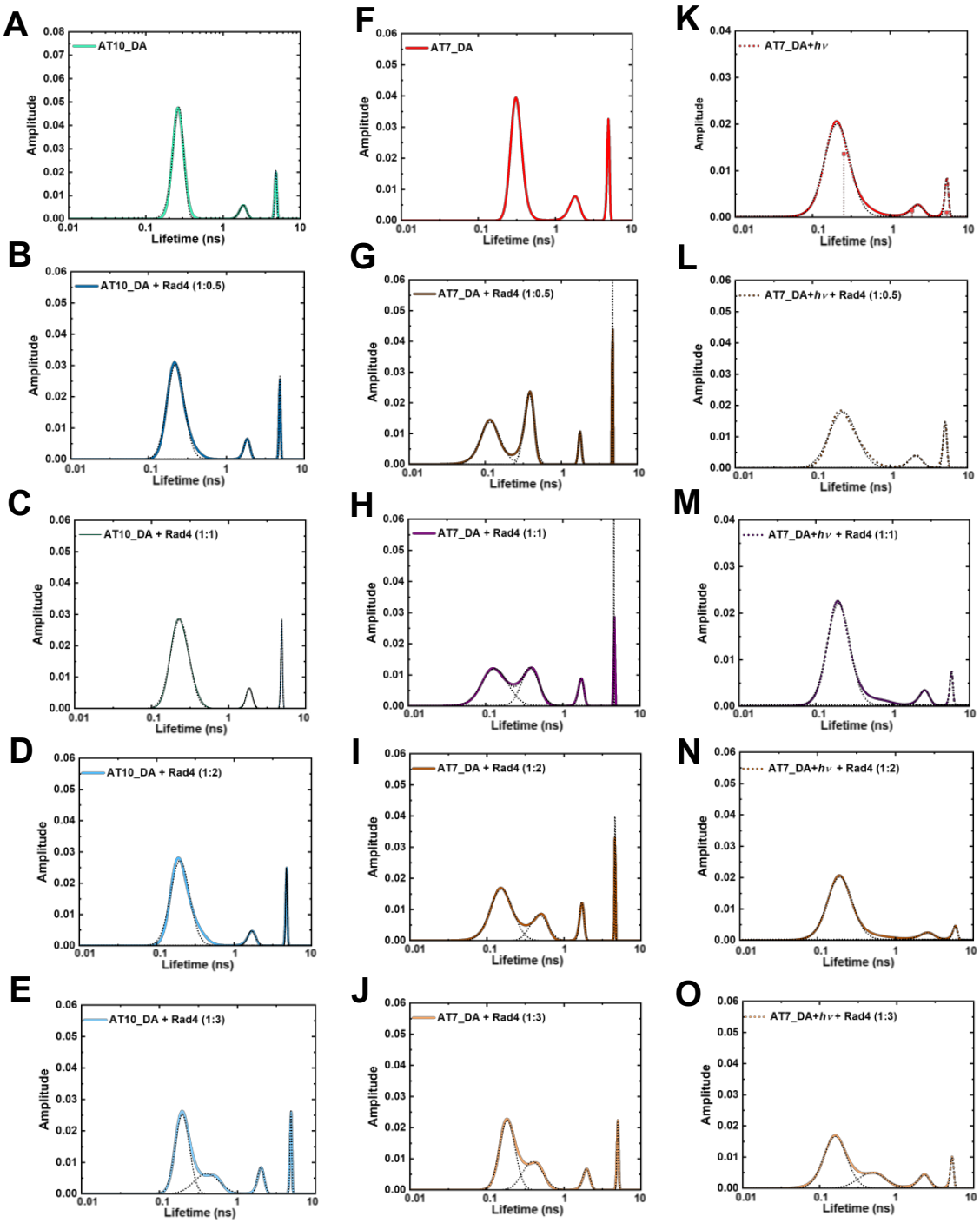

Figure S11. MEM lifetime distributions for samples prepared with varying DNA:Rad4 ratios. **(A-E)** Unmodified DNA (AT10_DA):Rad4 ratios were varied as **(A)** 1:0, **(B)** 1:0.5 **(C)** 1:1, **(D)** 1:2, and **(E)** 1:3. **(F-J)** show corresponding data for NPOM-DNA (AT7_DA) and **(K-O)** for photo-cleaved NPOM-DNA (AT7_DA+$h\nu$: NPOM-DNA was photo-cleaved by 365 nm light for 2 min before adding Rad4).

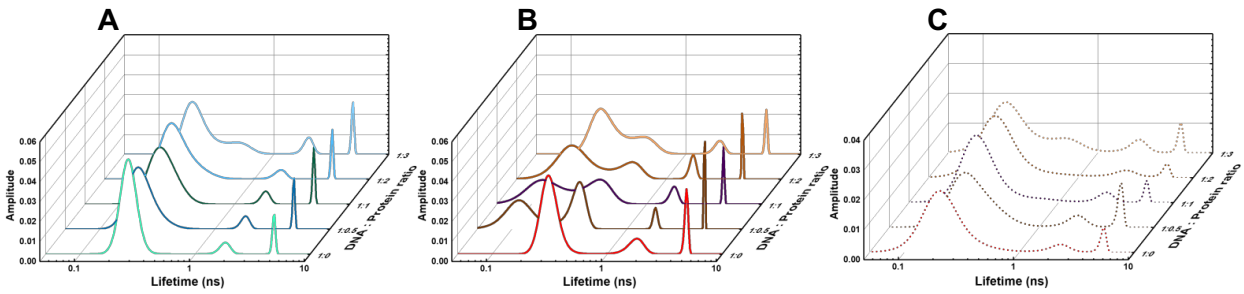

Figure S12. MEM lifetime distributions for samples prepared with varying DNA:Rad4 ratios. Data shown in Figure S11 are presented in 3-D graphs.

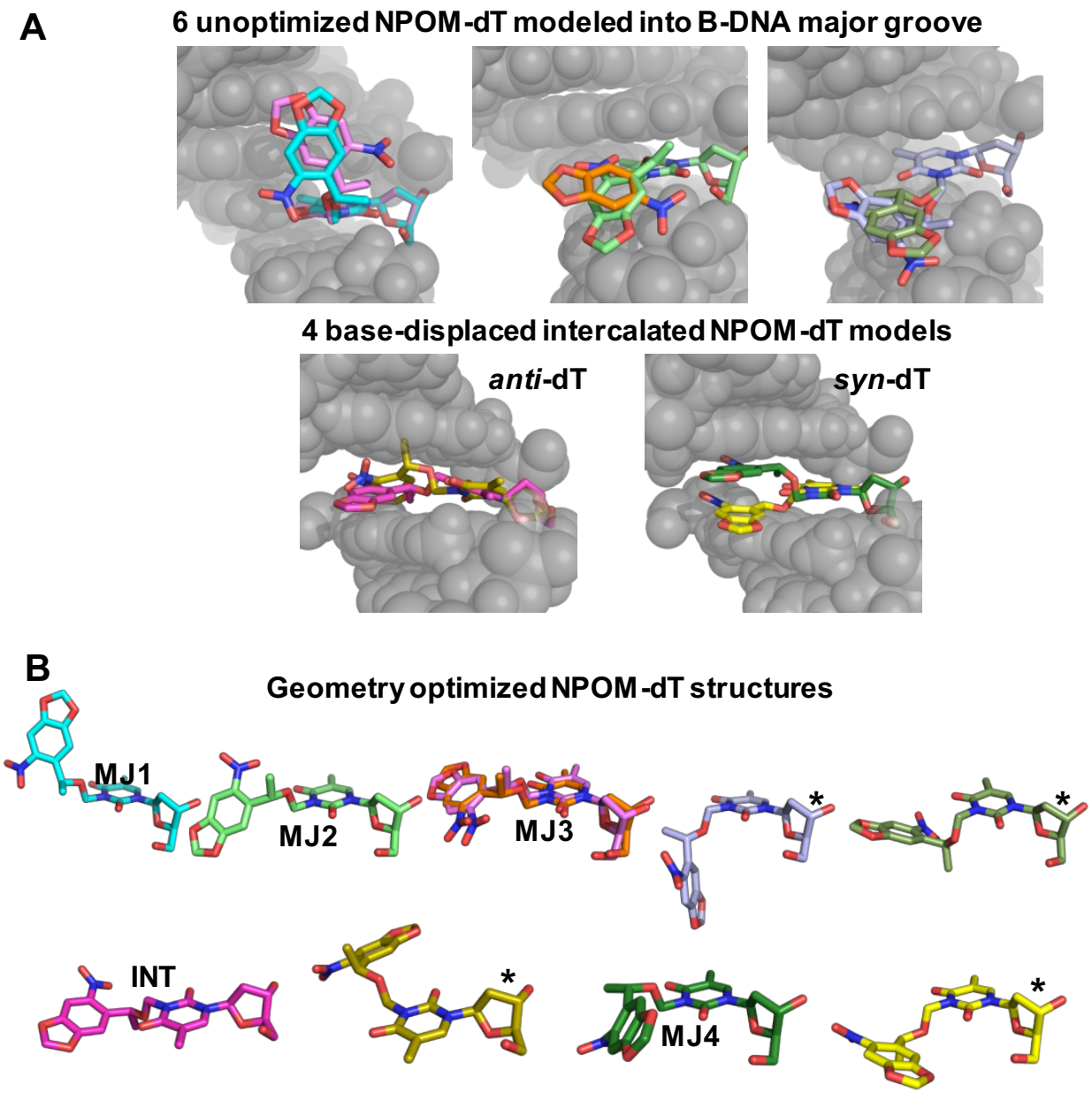

Figure S13. NPOM-dT nucleoside conformational searches and geometry optimized conformations. **(A)** Unoptimized NPOM-dT modeled in duplex B-DNA (gray spheres) as resulted from Stage 1 (see **Scheme 1**). NPOM-dT is shown in sticks with carbon atoms color-coded differently for each model. **(B)** Geometry-optimized NPOM-dT structures as resulted from Stage 2. Upon geometry optimization, two models converged (orange and light pink, MJ3). The NPOM-dT structures (MJ1, MJ2, MJ3, MJ4 and INT) are then modeled into B-DNA (Figure S14, Stage 3) as initial models for MD (Stage 4). The structures with * clash with neighboring base pairs in the context of duplex B-DNA and are not used for MD.

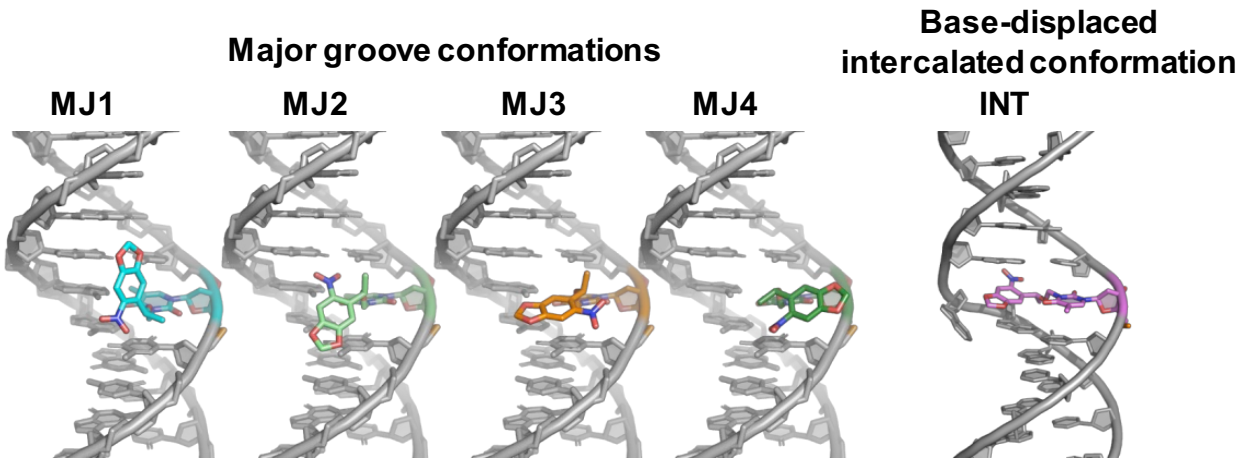

Figure S14. Initial models of NPOM-dT-containing DNA 13mers for MD simulations (indicated as Stage 3 in Scheme 1)**.** The NPOM-dT residues are color coded as in **Figure S13**.

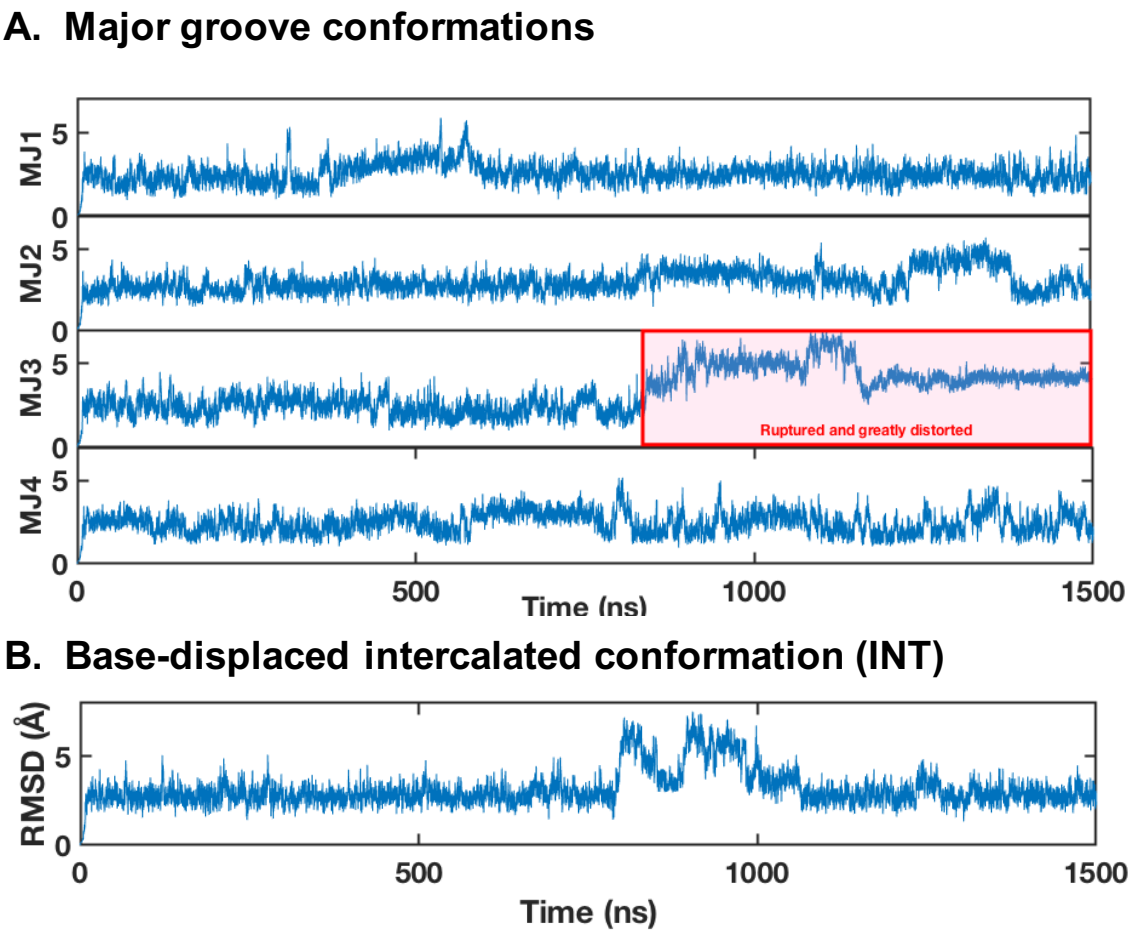

Figure S15. RMSDs for NPOM-dT-containing 6mers in the MD simulations (A and B) and best representative structures (C). The root-mean-squared deviation (RMSD) values are for the heavy atoms of the 6-mer sequence between the designed FRET base pair steps excluding the lesion-containing nucleotide. The best representative structures are for the two predominant major groove rotamers and one base-displaced intercalated conformation, shown in **Figure 6** (Stage 4 in Scheme 1).

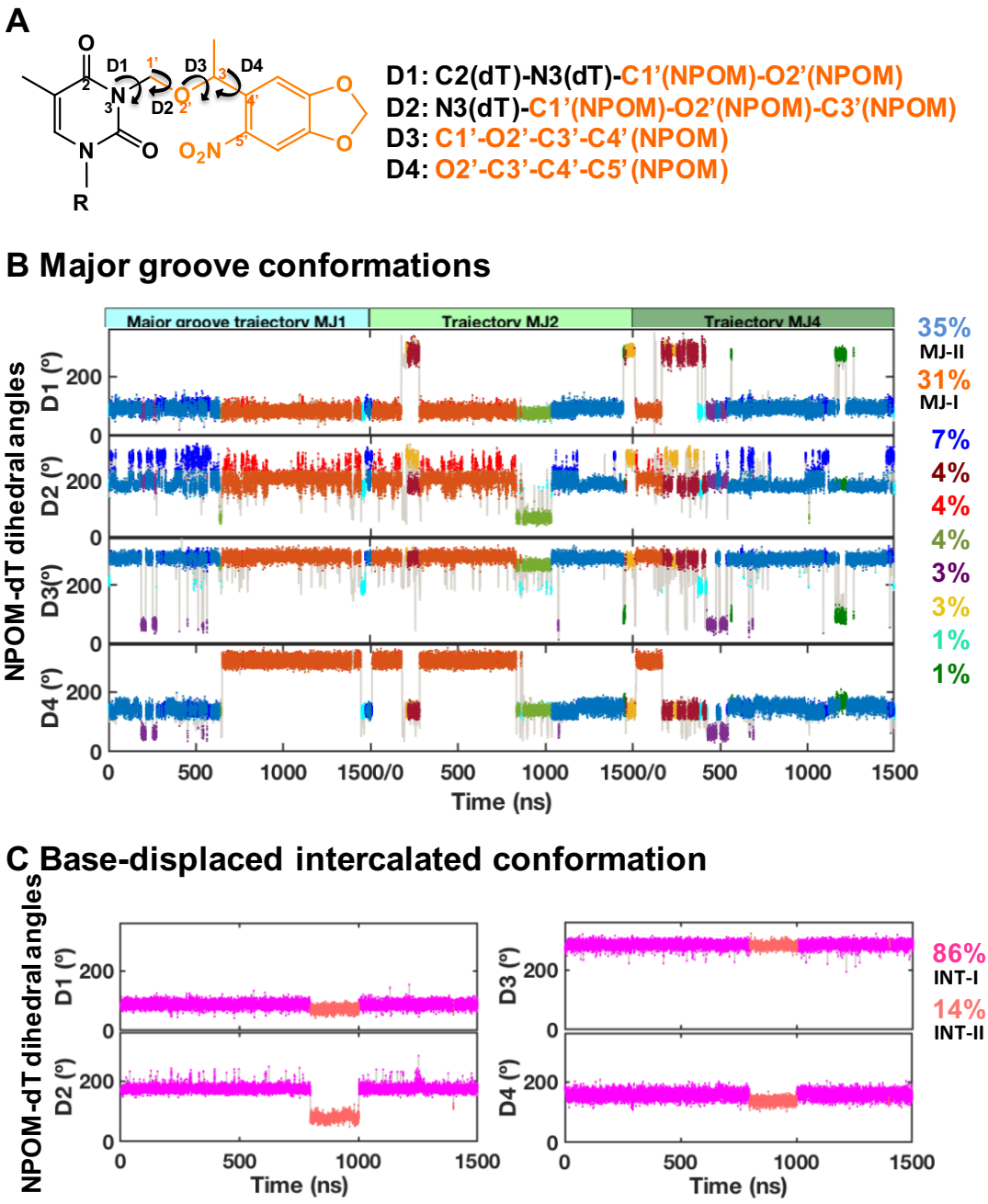

Figure S16. Conformational clusters of the NPOM-dT based on the dihedral angles between NPOM rings and dT. (A) The definition of dihedral angles between NPOM rings and dT. **(B)** The dihedral angle values and clusters of the NPOM-dT in the combined MD derived ensembles (MJ1, MJ2, and MJ4, Figures S14 and S15) of the major groove conformational family. **(C)** The dihedral angle values and clusters of the NPOM-dT in the MD derived ensembles of the base-displaced intercalated conformational family. Population fraction for each cluster (over 1%) is color-coded and given on the right.

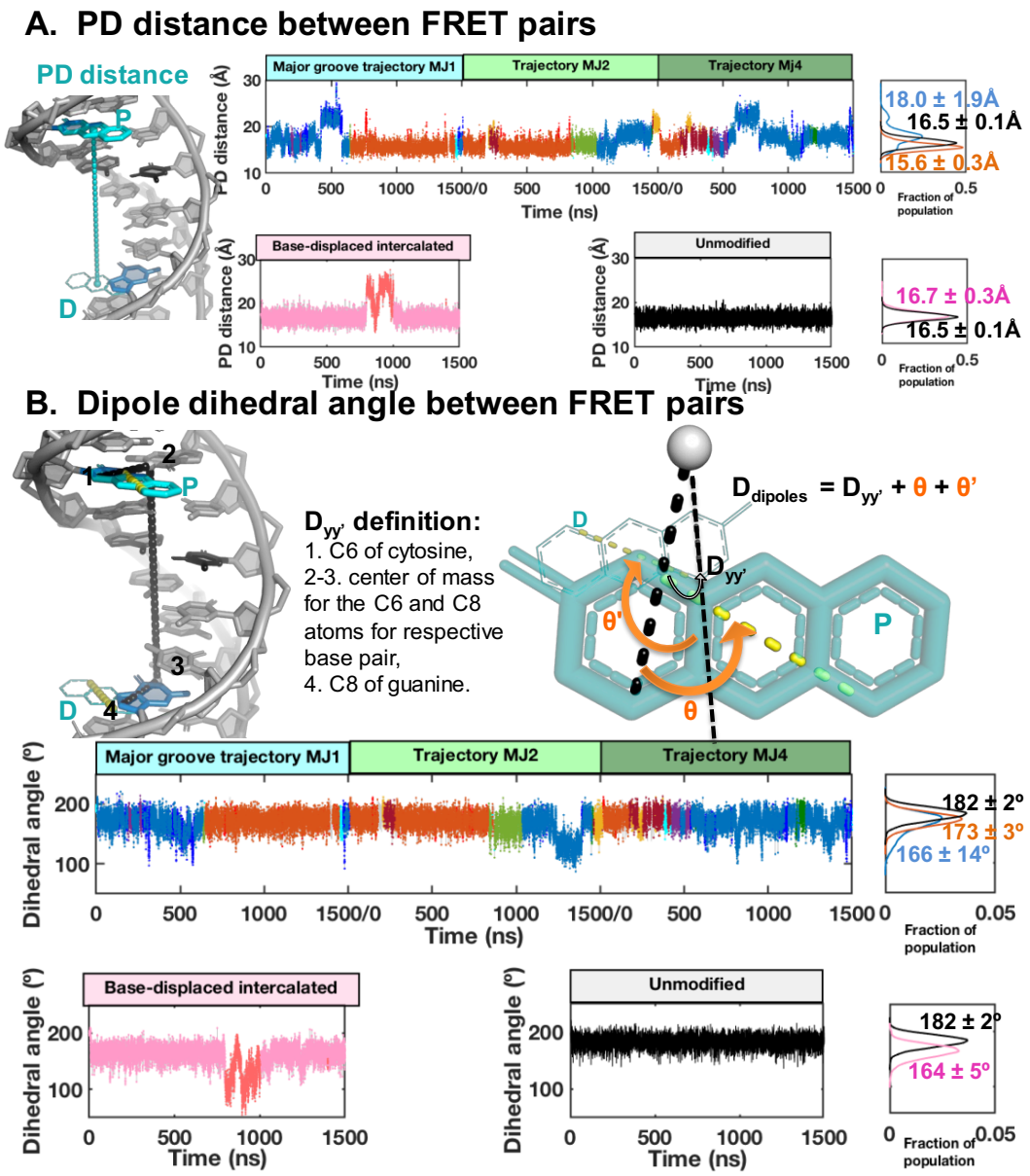

Figure S17. The distances and the dipole dihedral angles between modeled FRET pairs. The distances **(A)** and dipole dihedral angles **(B)** between FRET pairs are illustrated in the best-representative structure of unmodified DNA, and their values along the MD trajectories are shown. The values are color coded as in Figure S16 for each conformation. The kernel distributions of the values for predominant conformations are shown on the right labeled with respective mean and standard deviation for the block averaged values (see Supporting Methods). Kernel densities for the values are calculated using the ksdensity function with 200 bins in MATLAB 7.10.0 (The MathWorks, Inc.), and are representative of the population distributions over the range of each property.

Supporting References

1. M. J. Frisch, G. W. Trucks, H. B. Schlegel, G. E. Scuseria, M. A. Robb, J. R. Cheeseman, G. Scalmani, V. Barone, G. A. Petersson, H. Nakatsuji, X. Li, M. Caricato, A. Marenich, J. Bloino, B. G. Janesko, R. Gomperts, B. Mennucci, H. P. Hratchian, J. V. Ortiz, A. F. Izmaylov, J. L. Sonnenberg, D. Williams-Young, F. Ding, F. Lipparini, F. Egidi, J. Goings, B. Peng, A. Petrone, T. Henderson, D. Ranasinghe, V. G. Zakrzewski, J. Gao, N. Rega, G. Zheng, W. Liang, M. Hada, M. Ehara, K. Toyota, R. Fukuda, J. Hasegawa, M. Ishida, T. Nakajima, Y. Honda, O. Kitao, H. Nakai, T. Vreven, K. Throssell, J. A. J. Montgomery, J. E. Peralta, F. Ogliaro, M. Bearpark, J. J. Heyd, E. Brothers, K. N. Kudin, V. N. Staroverov, T. Keith, R. Kobayashi, J. Normand, K. Raghavachari, A. Rendell, J. C. Burant, S. S. Iyengar, J. Tomasi, M. Cossi, J. M. Millam, M. Klene, C. Adamo, R. Cammi, J. W. Ochterski, R. L. Martin, K. Morokuma, O. Farkas, J. B. Foresman and D. J. Fox, *Gaussian 09 Revision E.01*, Gaussian Inc.: Wallingford CT, 2016.
2. J. A. Maier, C. Martinez, K. Kasavajhala, L. Wickstrom, K. E. Hauser and C. Simmerling, *J Chem Theory Comput*, 2015, **11**, 3696-3713.
3. J. Wang, R. M. Wolf, J. W. Caldwell, P. A. Kollman and D. A. Case, *J Comput Chem*, 2004, **25**, 1157-1174.
4. Y. C. Myung and S. Han, *Bulletin of the Korean Chemical Society*, 2010, **31**, 2581-2587.
5. P. Cieplak, W. D. Cornell, C. Bayly and P. A. Kollman, *J. Comput. Chem.* , 1995, **16**, 1357-1377.
6. W. L. Jorgensen, J. Chandrasekhar, J. D. Madura, R. W. Impey and M. L. Klein, *J Chem Phys*, 1983, **79**, 926-935.
7. D. A. Case, I. Y. Ben-Shalom, S. R. Beozell, D. S. Cerutti, I. Cheatham, T.E.,, V. W. D. Cruzeiro, T. A. Darden, R. E. Duke, D. Ghoreishi, M. K. Gilson, H. Gohlke, A. W. Goetz, D. Greene, R. Harris, N. Homeyer, Y. Huang, S. Izadi, A. Kovalenko, T. Kurtzman, T. S. Lee, S. LeGrand, P. Li, C. Lin, J. Liu, T. Luchko, R. Luo, D. J. Mermelstein, K. M. Merz, Y. Miao, G. Monard, C. Nguyen, H. Nguyen, I. Omelyan, A. Onufriev, F. Pan, R. Qi, D. R. Roe, A. Roitberg, C. Sagui, S. Schott-Verdugo, J. Shen, C. L. Simmerling, J. Smith, R. Salomon-Ferrer, J. Swails, R. C. Walker, J. Wang, H. Wei, R. M. Wolf, X. Wu, L. Xiao and D. M. York, *AMBER 2018*, University of California, San Francisco: CA, 2018.
8. T. Darden, D. York and L. Pedersen, *J Chem Phys*, 1993, **98**, 10089-10092.
9. R. J. Loncharich, B. R. Brooks and R. W. Pastor, *Biopolymers*, 1992, **32**, 523-535.
10. H. J. C. Berendsen, J. P. M. Postma, W. F. Vangunsteren, A. Dinola and J. R. Haak, *J Chem Phys*, 1984, **81**, 3684-3690.
11. J. P. Ryckaert, G. Ciccotti and H. J. C. Berendsen, *J Comput Phys*, 1977, **23**, 327-341.
12. S. Xia, J. Beckman, J. Wang and W. H. Konigsberg, *Biochemistry*, 2012, **51**, 4609-4617.
13. S. Preus, K. Kilsa, F. A. Miannay, B. Albinsson and L. M. Wilhelmsson, *Nucleic Acids Res*, 2013, **41**, e18.
14. H. Flyvbjerg and H. G. Petersen, *J Chem Phys*, 1989, **91**, 461-466.
15. W. Yang, R. Bitetti-Putzer and M. Karplus, *J Chem Phys*, 2004, **120**, 2618-2628.